

## Article

# 4-Nonylphenol effects on rat testis and sertoli cells determined by spectrochemical techniques coupled with chemometric analysis

Duan, Peng, Liu, Bisen, Medeiros-De-morais, Camilo De Ielis, Zhao, Jing, Li, Xiandong, Tu, Jian, Yang, Weiyinxue, Chen, Chunling, Long, Manman, Feng, Xiaobing, Martin, Francis L and Xiong, Chengliang

Available at <http://clock.uclan.ac.uk/24909/>

*Duan, Peng, Liu, Bisen, Medeiros-De-morais, Camilo De Ielis ORCID: 0000-0003-2573-787X, Zhao, Jing, Li, Xiandong, Tu, Jian, Yang, Weiyinxue, Chen, Chunling, Long, Manman et al (2019) 4-Nonylphenol effects on rat testis and sertoli cells determined by spectrochemical techniques coupled with chemometric analysis. Chemosphere, 218 . pp. 64-75. ISSN 0045-6535*

It is advisable to refer to the publisher's version if you intend to cite from the work.

<http://dx.doi.org/10.1016/j.chemosphere.2018.11.086>

For more information about UCLan's research in this area go to <http://www.uclan.ac.uk/researchgroups/> and search for <name of research Group>.

For information about Research generally at UCLan please go to <http://www.uclan.ac.uk/research/>

All outputs in CLoK are protected by Intellectual Property Rights law, including Copyright law. Copyright, IPR and Moral Rights for the works on this site are retained by the individual authors and/or other copyright owners. Terms and conditions for use of this material are defined in the <http://clock.uclan.ac.uk/policies/>

1 **4-Nonylphenol effects on rat testis and Sertoli cells determined by**  
2 **spectrochemical techniques coupled with chemometric analysis**

3 Peng Duan<sup>1,2</sup>, Bisen Liu<sup>3</sup>, Camilo L. M. Morais<sup>4</sup>, Jing Zhao<sup>5</sup>, Xiandong Li<sup>6</sup>, Jian Tu<sup>7</sup>,  
4 Weiyngxue Yang<sup>3</sup>, Chunling Chen<sup>3</sup>, Manman Long<sup>3</sup>, Xiaobing Feng<sup>3</sup>, Francis L.  
5 Martin<sup>4,¶</sup>, Chengliang Xiong<sup>1,8,¶</sup>

6 *<sup>1</sup>Family Planning Research Institute, Tongji Medical College, Huazhong University of*  
7 *Science and Technology, Wuhan 430030, China; <sup>2</sup>Center for Reproductive Medicine,*  
8 *Xiangyang No. 1 People's Hospital, Hubei University of Medicine, Xiangyang 441000,*  
9 *China; <sup>3</sup>Department of Epidemiology and Biostatistics, School of Public Health,*  
10 *Tongji Medical College, Huazhong University of Science and Technology, Wuhan,*  
11 *Hubei, China; <sup>4</sup>School of Pharmacy and Biomedical Sciences, University of Central*  
12 *Lancashire, Preston PR1 2HE, UK; <sup>5</sup>Department of Epidemiology and Health*  
13 *Statistics, School of Public Health, Medical College, Wuhan University of Science and*  
14 *Technology, Wuhan 430030, China; <sup>6</sup>Department of Clinical Laboratory, Taihe*  
15 *Hospital, Hubei University of Medicine, Shiyan 442000, China; <sup>7</sup>Reproductive*  
16 *medicine center, Maternal and Child Health Care Hospital of Yueyang City, Yueyang*  
17 *414000, China; <sup>8</sup>Center for Reproductive Medicine, Wuhan Tongji Reproductive*  
18 *Medicine Hospital, 128 Sanyang Road, Wuhan 430013, China*

19

20 ¶ **Corresponding authors:**

21 ¶ **Chengliang Xiong**, Family Planning Research Institute, Tongji Medical College,  
22 Huazhong University of Science and Technology, 13 Hangkong Road, 430030 Wuhan,  
23 Hubei Province, China. Tel: +86-0278-83692651; E-mail: [clxiong951@sina.com](mailto:clxiong951@sina.com).

24 ¶ **Francis L. Martin**, School of Pharmacy and Biomedical Sciences, University of  
25 Central Lancashire, Preston PR1 2HE, UK. Tel: +44 (0)-1772 89-6482; E-mail:  
26 [flmartin@uclan.ac.uk](mailto:flmartin@uclan.ac.uk)

27 **Abstract**

28 Herein, vibrational spectroscopy has been applied for qualitative identification of  
29 biomolecular alterations that occur in cells and tissues following chemical treatment.  
30 Towards this end, we combined attenuated total reflection Fourier-transform infrared  
31 (ATR-FTIR) and Raman spectroscopy to assess testicular toxicology after  
32 4-nonylphenol (NP) exposure, an estrogenic endocrine disruptor affecting testicular  
33 function in rats and other species. Rats aged 21, 35 or 50 days received NP at  
34 intra-peritoneal doses of 0, 25, 50 or 100 mg/kg for 20 consecutive days. Primary  
35 Sertoli cells (SCs) were treated with NP at various concentrations (0, 2.5, 5, 10 or 20  
36  $\mu\text{M}$ ) for 12 h. Post-exposure, testicular cells, interstitial tissue and SCs were  
37 interrogated respectively using spectrochemical techniques coupled with multivariate  
38 analysis. Distinct biomolecular segregation between the NP-exposed samples *vs.*  
39 control were observed based on infrared (IR) spectral regions of  $3200\text{-}2800\text{ cm}^{-1}$  and  
40  $1800\text{-}900\text{ cm}^{-1}$ , and the Raman spectral region of  $1800\text{-}900\text{ cm}^{-1}$ . For *in vivo*  
41 experiments, the main wavenumbers responsible for segregation varied significantly  
42 among the three age classes. The main IR and Raman band differences between  
43 NP-exposed and control groups were observed for Amide (proteins), lipids and  
44 DNA/RNA. An interesting finding was that the peptide aggregation level, Amide  
45 I-to-Amide II ratio, and phosphate-to-carbohydrate ratio were considerably reduced in  
46 *ex vivo* NP-exposed testicular cells or SCs *in vitro*. This study demonstrates that  
47 ATR-FTIR and Raman spectroscopy techniques can be applied towards analysing  
48 NP-induced testicular biomolecular alterations.  
49

50 **Highlights**

51 • The extent of testicular damage was assessed by ATR-FTIR and Raman  
52 spectroscopy

53 • 4-Nonylphenol (NP) exposure-induced testicular toxicity is associated with  
54 biomolecular alterations

55 • The biomolecular alterations by the age at which NP exposure started

56

57

58 **Keywords:** 4-nonylphenol exposure, testicular toxicity, Sertoli cells, ATR-FTIR  
59 spectroscopy, Raman spectroscopy, multivariate analysis

60

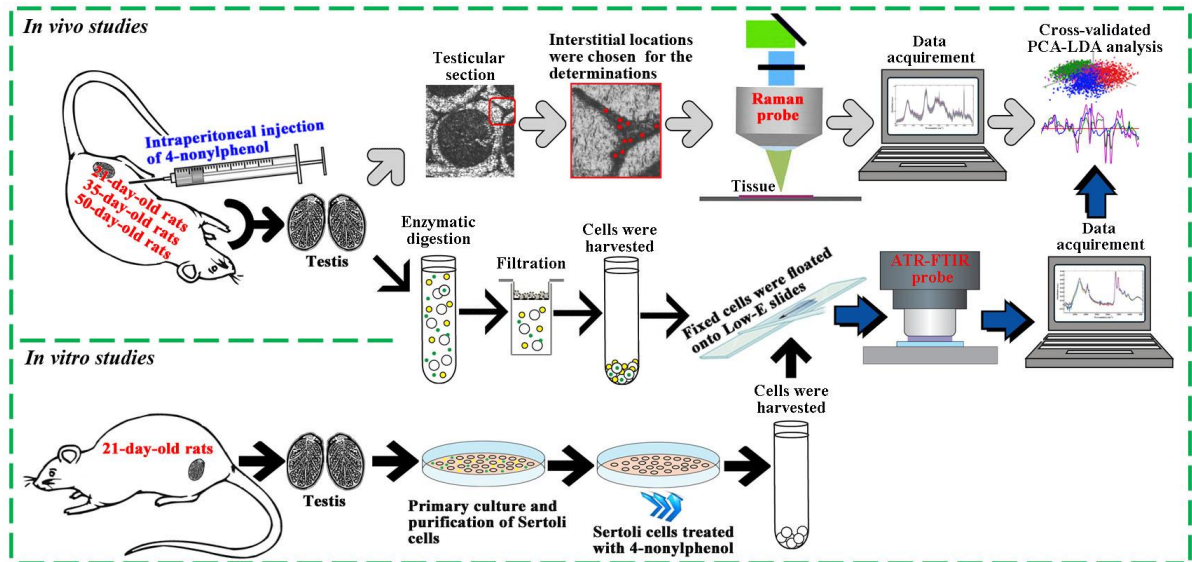
61 **Graphical abstract**

62

63

64

65



66

67

## 68 **1. Introduction**

69 Endocrine disrupting chemicals are natural or synthetic compounds, which are able to  
70 interfere with endocrine system and consequently cause various health problems in  
71 animals and human beings (Lee et al., 2013). One of the most frequently detected  
72 endocrine disrupting chemicals is 4-nonylphenol (NP), an environmental  
73 oestrogen-like chemical derived from nonylphenol ethoxylates (NPEOs), which are  
74 extensively used as non-surfactants in detergents, emulsifiers, wetting and dispersing  
75 agents, and pesticide formulations for the last 40 years (Soares et al., 2008; Iqbal and  
76 Bhatti, 2015). NP belongs to category 1 (clear evidence of endocrine disrupting  
77 effects in an intact organism) of the endocrine disrupter priority list (Wang et al.,  
78 2016). The occurrence of NP has been reported in different environmental  
79 compartments worldwide, as well as within humans and other biota (Fairbairn et al.,  
80 2016; Staniszewska et al., 2016; Wang et al., 2016; Diao et al., 2017; Lin et al., 2017;  
81 Peng et al., 2017). According to a study conducted in the Zumbro River watershed of  
82 United States, the concentration of NP was up to  $10^4$  ng/L (Fairbairn et al., 2016). In  
83 the Pearl River Estuary of China, NP was identified at concentrations ranging from  
84 233.04 to 3352.86 ng/L in surface water and 7.55 to 20.80 ng/g of dry weight (dw) in  
85 sediment (Diao et al., 2017). As regards exposure to wildlife and humans, high NP  
86 levels (111.2 ng/g dw) were determined in zooplankton off the Gulf of Gdansk  
87 (Southern Baltic) in the years 2011-2012 and, additionally, NP was found in cord  
88 blood plasma with a median concentration of 72.6 ng/mL in 208 children from Taiwan  
89 (Staniszewska et al., 2016; Lin et al., 2017). NP has also been detected in food, such  
90 as cereals and vegetables (Aparicio et al., 2017; Pastor-Belda et al., 2017). Due to its  
91 ubiquitous presence and known estrogenomimetic properties, there is a growing  
92 concern regarding the environmental fate and potential impacts of NP on human and  
93 ecosystem health (Li et al., 2013b).

94 NP has been found in various human tissues (Deng et al., 2010; Asimakopoulos  
95 et al., 2012) and to cause a wide range of reproductive and developmental toxicities in  
96 fish and mammals (Chapin et al., 1999; El-Sayed Ali et al., 2014; Duan et al., 2016a;

97 Duan et al., 2017b). Male reproductive system toxicity is one of the prominent  
98 adverse effects of NP (Noorimotlagh et al., 2017). Evidence that NP could exert  
99 estrogenic actions and disturb hormonal homeostasis has arisen from studies in male  
100 rats models (Chapin et al., 1999; Duan et al., 2017a). Our previous studies found that  
101 pre-pubertal exposure to NP in rats induced reproductive dysfunction during  
102 adulthood (Duan et al., 2016a; Huang et al., 2016). NP treatment affects  
103 spermatogenesis, sperm function and morphology (El-Sayed Ali et al., 2014; Cheng et  
104 al., 2017; Duan et al., 2017a). When treated with  $\geq 50$  mg NP/kg, the seminiferous  
105 tubules exhibit a hollow tendency and the levels of apoptosis of testicular cells  
106 increase (Duan et al., 2016a; Huang et al., 2016; Duan et al., 2017a). NP has been  
107 shown to trigger apoptosis and autophagy in Sertoli cells (Huang et al., 2016; Duan et  
108 al., 2017b; Su et al., 2018). Additionally, Jambor *et al* confirmed the inhibitory effects  
109 of 5.0 mg NP/mL on mice Leydig cells *in vitro* (Jambor et al., 2017). The results of  
110 these studies converge to suggest that NP is a potent testicular toxicant. The multiple  
111 mechanisms responsible for testicular toxicity of NP involve oxidative stress,  
112 modulation of MAPK/Akt/AMPK/mTOR signalling, autophagic and apoptotic  
113 pathways (Liu et al., 2014; Duan et al., 2016b; Huang et al., 2016). Of note, the  
114 evidence of direct association between NP exposure and alterations in the  
115 biomolecular signatures of testicular cells remain limited.

116 Vibrational spectroscopy has attracted growing attention as a bio-analytical tool  
117 for biomedical research. The most commonly used methods include Fourier-transform  
118 infrared (FTIR) in transmission, transfectance or reflection modes; and Raman  
119 spectroscopy (Owens et al., 2014). Attenuated total reflection (ATR)-FTIR or Raman  
120 spectroscopies have many advantages over traditional molecular biology techniques  
121 (*e.g.*, ELISA, Western blotting, RT-PCR), since they are able to analyse samples in a  
122 non-destructive and label-free manner (Andrew Chan and Kazarian, 2016; Butler et  
123 al., 2016; Paraskevaidi et al., 2017b), with minimal sample preparation (Butler et al.,  
124 2016; Obinaju and Martin, 2016), and allowing a simultaneous analysis of a wide  
125 range of different biomolecules (Paraskevaidi et al., 2017b). In the past few years,

126 ATR-FTIR and Raman spectroscopy have been extensively applied in toxicology  
127 studies, including *in vivo* (Chen et al., 2015; Li et al., 2015; Obinaju and Martin, 2016)  
128 and *in vitro* tests (Obinaju et al., 2015; Li et al., 2016; Strong et al., 2016). In addition,  
129 their potential for disease diagnosis has also been demonstrated in many publications  
130 (Gajjar et al., 2012; Owens et al., 2014; Lima et al., 2015; Paraskevaidi et al., 2017b).

131 ATR-FTIR spectroscopy measures the energy absorbed by functional groups  
132 within a sample after exposure to IR radiation and generates a spectrum with peaks  
133 related to chemical structure of particular entities, *e.g.*, lipids  $\sim 1740\text{ cm}^{-1}$ , DNA  
134  $\sim 1080\text{ cm}^{-1}$ , Amide I and II  $\sim 1650$  and  $1550\text{ cm}^{-1}$ , respectively. Such entities are  
135 mainly present in the  $1800\text{-}900\text{ cm}^{-1}$  region (known as the “biochemical fingerprint”  
136 region) (Li et al., 2016; Strong et al., 2016). In contrast, Raman spectroscopy exploits  
137 the phenomena of inelastic scattering to detect chemical bonds (Butler et al., 2016).  
138 Using Raman microspectroscopy, it is possible to image individual cells on the  
139 subcellular level (Eberhardt et al., 2015), making it an excellent technique to detect  
140 alterations in specific cells. The combined application of ATR-FTIR and Raman  
141 spectroscopy can offer complementary structural information about the same sample.

142 Therefore, in the present study, both ATR-FTIR and Raman spectroscopy were  
143 employed to detect biomolecular alterations in testis from NP-treated rats of different  
144 ages and NP-treated sertoli cells *in vitro*. Following spectroscopic measurements,  
145 spectral data were analysed using principal component analysis followed by linear  
146 discriminant analysis (PCA-LDA), which generates scores plots in two- or  
147 three-dimensional spaces and allows the construction of cluster vectors (Heppenstall  
148 et al., 2013) for data visualization. The aim of this study was to determine the  
149 NP-induced effects on biomolecular parameters of testis in a dose- and age-related  
150 manner.

151

152

153

## 154 **2. Materials and methods**



## 155 **2.1 Primary culture of rat testicular Sertoli cells (SCs) and their identification**

156 Primary Sertoli cell (SC) cultures were prepared from testis of 18- to 21-day-old rat,  
157 as previously described (Duan et al., 2016b; Duan et al., 2017b), with modifications.  
158 Briefly, testis were digested in DMEM/F12 (1:1) medium (Hyclone, USA) containing  
159 0.25% trypsin (Sigma, USA) and 0.5 mg/mL Deoxyribonuclease I (DNase I) (Sigma,  
160 USA) for 30 min with 75 cycles/min shaking in a water bath at 37°C. The digested  
161 tissues were centrifuged and washed with D-Hanks twice, and the washed tubular  
162 pellets were suspended in DMEM/F12 medium containing 1 mg/mL collagenase I, 0.5  
163 mg/mL DNase I and 1 mg/mL hyaluronidase (Sigma, USA) at 37°C for 20 min with  
164 120 cycles/min shaking. Thereafter, the suspension was filtered through a 200-mesh  
165 cell sieve and the cells were washed twice with D-Hanks. Primary cells were  
166 re-suspended in DMEM/F12 medium supplemented with 1 % penicillin-streptomycin  
167 (Beyotime, China) and seeded in 6-well plates at a density of  $1 \times 10^6$  cells per well.  
168 Cells were maintained in a humidified atmosphere of 95% air-5% CO<sub>2</sub> at 35°C and  
169 the serum-free medium was changed at 24 h intervals. On Day 3 of culture,  
170 contaminating spermatogenic cells were lysed with a hypotonic solution of 20 mM  
171 Tris-HCl (pH 7.4) for 3 min, washed with medium twice, and then incubated with  
172 fresh medium. After 24 h, SCs were incubated by immunofluorescence with Wilms  
173 tumor 1 (WT1) (Abcam, UK) (Abcam, UK) antibody to detect the purity of SCs [see  
174 Electronic Supplementary Information (ESI) **Figure S1**]. SCs with the purity of >90%  
175 and good cellular morphology were used in this experimental work.

## 176 **2.2 Exposure treatments and cell viability**

177 NP (CAS no. 84852-15-3) (Leicestershire, UK) was dissolved in dimethylsulfoxide  
178 (DMSO) (Sigma, USA) as stock solution and diluted with DMEM/F12 (1:1) medium  
179 to different concentrations before being added to the SCs in culture. The final DMSO  
180 concentration in the medium was not more than 0.1% (v/v), which did not affect the  
181 viability of SCs. Control SCs were cultured with 0.1% DMSO.

182 In this study, the dosages of NP ranging from 2.5 to 20  $\mu$ M were based on our

183 previous studies (Duan et al., 2016b; Huang et al., 2016; Duan et al., 2017b). SCs  
184 were seeded in a 96-well plate and treated with various concentrations of NP (0, 2.5, 5,  
185 10 or 20  $\mu\text{M}$ ) for 6, 12 or 24 h. Cellular viability was assessed using a CCK-8 kit  
186 (Beyotime, Shanghai, China), as previously mentioned (Duan et al., 2016b). Cell  
187 viability index was calculated using the following formula:

$$188 \quad \text{Cell viability \%} = [(A_{450} \text{ sample} - \text{background}) / (A_{450} \text{ control} - \text{background})] \times$$

189 100%

190 Each experiment was repeated six times.

### 191 **2.3 Sertoli cell preparation for ATR-FTIR spectroscopy**

192 After treatment with different concentrations of NP for 12 h, the cells were washed  
193 with D-Hanks, trypsinized, and centrifuged at 800 rpm for 5 minutes at 4°C.  
194 Following this, cell pellets were immediately re-suspended in 4% paraformaldehyde  
195 (PFA) (Beyotime, China) for 30 min, washed with D-Hanks twice, floated onto  
196 infrared-reflective Low-E glass slides (Kevley Technologies, USA), and then air-dried  
197 at room temperature for 24 h before ATR-FTIR spectroscopy. The experiments were  
198 repeated six times for each NP treatment.

### 199 **2.4 Animal experiment protocol and sample collection**

200 Male Sprague-Dawley (SD) rats were obtained from Tongji Medical College Animal  
201 Centre (Wuhan, China). All rats were housed in a specific pathogen-free animal  
202 facility with unrestricted access to standard rodent chow diet and tap water in  
203 experimental animal centre of Tongji Medical College (Wuhan, China). The animal  
204 facility conditions were as follows: temperature  $22 \pm 2^\circ\text{C}$ ; humidity  $60 \pm 5\%$ ; artificial  
205 12:12-h light-dark cycle: light on at 06:00 am. All experimental procedures involving  
206 the use of rats in this study were reviewed and approved by the Animal Care and Use  
207 Committee of Tongji Medical College, Huazhong University of Science and  
208 Technology.

209 Pre-puberty is considered the critical time for male sexual differentiation in the  
210 SD rat (Lu et al., 2016). Most cells in the seminiferous tubules at pre-puberty are  
211 Sertoli cells. Adolescence is a unique period of enhanced vulnerability to the  
212 reproductive toxicity caused by endocrine disrupting chemicals because of their  
213 interference effects on the onset of spermatogenesis. The entire process of  
214 spermatogenesis is newly established during the period of young adulthood. To  
215 explore the effects of NP on the biomolecular composition of testicular cells at  
216 different age stages, in the present study, NP dissolved in corn oil (Sigma, USA) free  
217 of antioxidants was intraperitoneally injected into prepuberty (21 days),  
218 peri-adolescent (35 days) and young adult (50 days) rats. Twenty-four rats from each  
219 age-class were divided randomly into four groups consisting of six rats each: vehicle  
220 control group (only corn oil), low-dose NP group (25 mg/kg body weight),  
221 middle-dose NP group (50 mg/kg body weight) and high-dose NP group (100 mg/kg  
222 body weight). The injections were administered from 8:30 am to 11:30 am every other  
223 day for 20 consecutive days. These doses and times were chosen on the basis of  
224 previous studies (Duan et al., 2016a; 2017a; Huang et al., 2016). The dosing volume  
225 was set at 5 ml/kg body weight in all groups. Body weights of each rat were recorded  
226 before NP administration.

227 Two days after the last injections, all animals were weighted and sacrificed by  
228 decapitation, their testes were dissected out and immediately weighed for calculation  
229 of testis index. The left testis of each rat was used for haematoxylin and eosin (H&E)  
230 staining and spectroscopic analysis, and the right testis were flash-frozen in liquid  
231 nitrogen and then stored at 80°C until use.

## 232 **2.5 ATR-FTIR spectroscopic analysis of Sertoli cells and testicular cells**

233 Cell samples on Low-E glass slides were analysed using a Tensor 27 FTIR  
234 spectrometer equipped with a Helios ATR attachment containing a diamond crystal  
235 (~250 × 250 µm sampling area) (Bruker Optics Ltd., Coventry, UK). The details of  
236 operation procedure and spectral acquisition were the same as our previous reports  
237 (Baker et al., 2014; Jin et al., 2017; Paraskevaidi et al., 2017b). Briefly, the parameters

238 for recording the IR spectra were set at spectral range of 4000-400  $\text{cm}^{-1}$ , 32 co-added  
239 scans, 8  $\text{cm}^{-1}$  resolution and  $2\times$  zero-filling to maximize the signal-to-noise ratio. Ten  
240 spectra were acquired from different sites of each cell sample to minimize bias. The  
241 ATR crystal was cleaned with distilled water and dried with soft tissue, and a new  
242 background spectrum was taken prior the measurement of each next cell sample.  
243 Subsequently, spectra were converted to absorbance using Bruker OPUS software. IR  
244 spectra were pre-processed using IRootLab toolbox (<http://trevisanj.github.io/irootlab/>)  
245 running on MATLAB R2010a (The MathWorks, Inc., US) (Baker et al., 2014;  
246 Paraskevaidi et al., 2017b). Raw spectra were cut, baseline-corrected and normalized  
247 over the 3500-750  $\text{cm}^{-1}$  region.

## 248 **2.6 Tissue section preparation for Raman spectroscopic analysis**

249 The half-left testis of each rat were fixed in 4% PFA at 4°C overnight, embedded in  
250 paraffin, sectioned for 10  $\mu\text{m}$  thickness and then transferred onto a slide covered with  
251 aluminum foil (Li et al., 2017). The paraffin-embedded testicular sections were  
252 routinely de-paraffinized with xylene and a graded series of ethanol (100%, 90%, 80%  
253 and 70%) for 2 min each. Testicular sections were air-dried at room temperature for  
254 24 h and analysed by Raman spectroscopy. Raman spectra of testicular interstitial  
255 tissue were recorded using an InVia Renishaw Raman spectrometer with a 785 nm  
256 diode laser (Renishaw plc, UK), which has recently been described in more detail  
257 (Butler et al., 2016; Li et al., 2017). Briefly, the Raman system was calibrated using  
258 the 520  $\text{cm}^{-1}$  band of a silicon wafer for assessing wavenumber shifts. An attached  
259 microscope (Leica Microsystems, Milton Keynes, UK) with  $\times 50$  objective (0.75  
260 numerical aperture;  $\sim 1 \mu\text{m}$  spatial resolution) was utilized for point-mapping of  
261 interstitial tissue. All point spectra were collected using 100% laser power (26 mW at  
262 sample), 15 s exposure time and 1 accumulation within the 1800~900  $\text{cm}^{-1}$  spectral  
263 range, and approximately 100 spectra were obtained from different sites of testicular  
264 interstitial tissue from each rat. Each acquired raw spectrum was pre-processed by  
265 rubberband baseline correction and normalization to the Amide I peak using  
266 MATLAB (Butler et al., 2016; Li et al., 2017).

## 267 **2.7 Multivariate data analysis**

268 After pre-processing, principal component analysis coupled with linear discriminant  
269 analysis (PCA-LDA) was applied to the resulting dataset to identify between-category  
270 segregation. The output data derived from PCA-LDA were extracted and represented  
271 in the form of scores plots and cluster vectors. PCA-LDA cluster vectors were  
272 developed to identify the distinguishing wavenumbers responsible for separating the  
273 control from the other categories (Riding et al., 2012; Li et al., 2013a). Herein, the  
274 NP-induced biomolecular alterations were determined by setting the control at the  
275 origin with a zero coefficient value, which represented no biochemical alteration. One  
276 cluster vector was generated through the mean of each group. For the cluster vectors  
277 of all NP treatment groups vs. the corresponding control (line at origin), the extent of  
278 peak deviation away from the origin is proportional to the extent of biomolecular  
279 alteration. In this case, we were able to detect the prominent wavenumbers that mainly  
280 contributed to category segregation and then explain biomolecular differences  
281 between NP-treated vs. control groups. PCA-LDA-based spectral classification was  
282 performed using leave-one-out cross-validation as previously described (Li et al.,  
283 2015; Paraskevaidi et al., 2017b).

## 284 **2.8 Statistical analysis**

285 The results were expressed as the means  $\pm$  standard deviation (SD). Statistical  
286 analysis across multiple groups was performed using a one-way analysis of variance  
287 (ANOVA), followed by Fisher's LSD post-hoc test for homogeneity of variance and  
288 Dunnett's T3 post-hoc test for heterogeneity of variance. The effects of both NP  
289 concentrations and exposure age, as independent factors, and the interaction effects  
290 between the factors were tested by two-way ANOVA. All significance testing were  
291 carried out in SPSS software version 12.0 (SPSS, Chicago, IL, USA). Two-sided  
292 *P*-values of  $<0.05$  and  $<0.001$  were considered as statistically significant or highly  
293 significant, respectively. Scatter plots and bar graphs were done using GraphPad  
294 PRISM Version 4.0 (San Diego, CA, USA).

## 295 **3. Results**

### 296 **3.1 General and histopathological observations**

297 No mortality was observed in any of the treatment groups. As shown in **ESI Figure**  
298 **S2**, prepubertal, periadolescent and young adult exposure to NP did not affect final  
299 body weights, weight gain, testis weights or testis coefficient of rats with different  
300 ages ( $P>0.05$ ). No interaction effects between NP concentrations and NP-exposure  
301 life stages were observed regarding organ coefficient of testis (two-way ANOVA,  
302  $P_{interaction}=0.551$ ); however, age was a significant factor (effect of ages  $P<0.001$ ) (see  
303 **ESI Figure S3**). Body weights, measured at each time point between Day 0 and 20,  
304 were similar in NP-exposed and corresponding control animals ( $P>0.05$ , data not  
305 shown).

306 Testicular tissues of the control group within each age subgroup exhibited intact  
307 architecture with well-organized seminiferous tubules, while those from rats exposed  
308 to NP showed dose-dependent degenerative histological changes in the tubules in the  
309 form of vacuolation and loss of normal tubular architecture (see **ESI Figure S4**).

### 310 **3.2 ATR-FTIR spectroscopy detects NP-induced biomolecular alterations in testis** 311 **cells**

312 Herein, the IR spectral regions processed included the biochemical-cell fingerprint  
313 region ( $1800-900\text{ cm}^{-1}$ ) and the lipid region ( $3200-2800\text{ cm}^{-1}$ ) [**ESI Figure S5**]. The  
314 between-class covariance matrix using spectral data of these two regions highlights  
315 the structural and compositional variations of testicular cells between the NP-treated  
316 and control groups within each age-class (see **ESI Figure S6**). Projection of the  
317 spectral points in three-dimensional (3-D) spaces enables visualization of clustering  
318 patterns among categories. Cluster segregation between NP-treated and control  
319 categories at different age-classes is apparent in both  $1800-900\text{ cm}^{-1}$  region (**Figure**  
320 **1A**) and  $3200-2800\text{ cm}^{-1}$  region (**Figure 1B**).

321 Scores on linear discriminant 1 (LD1) space contain most of the variance in the  
322 spectral data and allow observation of a dose-response relationship. **Figure 1C-D**

323 shows that in all treatment groups, the NP-induced effects observed exhibit a  
324 dose-related response and differed significantly from the corresponding control group  
325 ( $P < 0.001$ ), except the 25 mg NP/kg treatment within the 50-day-old class at the lipid  
326 region ( $P > 0.05$ ). Two-way ANOVA demonstrates significant interaction effects  
327 between NP concentrations and NP-exposure life stages with respect to LD1 scores of  
328 both the 1800-900  $\text{cm}^{-1}$  and 3200-2800  $\text{cm}^{-1}$  regions ( $P < 0.001$ ) (see ESI Figure S7).  
329 Interestingly, there was no marked effect of age on the LD1 change of 3200-2800  $\text{cm}^{-1}$   
330 region (effect of ages  $P = 0.154$ ).

331 The derived cluster vectors plots comparing NP-treated rats to control in  
332 testicular cells show NP-induced changes associated with distinguishing IR  
333 wavenumbers (Figure 2). The IR peaks at 1200  $\text{cm}^{-1}$  (collagen), 1416  $\text{cm}^{-1}$  (proteins),  
334 1481  $\text{cm}^{-1}$  (protein conformation), 1504  $\text{cm}^{-1}$  (Amide II), 1670  $\text{cm}^{-1}$  (Amide I), and  
335 those associated with CH stretching vibrations of lipids (2816, 3028 and 3090  $\text{cm}^{-1}$ )  
336 were identified by the peak detector and are included in the cluster vectors plot of  
337 21-day-old class (Figure 2A). From the cluster vectors plot of the 35-day-old class  
338 (Figure 2B), there are highlighted IR peaks at 1111  $\text{cm}^{-1}$  (RNA), 1207  $\text{cm}^{-1}$  (collagen),  
339 1308  $\text{cm}^{-1}$  (Amide III), 1534  $\text{cm}^{-1}$  (modified guanine, Amide II), 1582  $\text{cm}^{-1}$  (Amide II),  
340 1667  $\text{cm}^{-1}$  (Amide I  $\beta$ -turns of proteins), 1732  $\text{cm}^{-1}$  (fatty acids) and 3055  $\text{cm}^{-1}$   
341 (stretching C-H). As depicted for the 50-day-old class in Figure 2C, distinguishing IR  
342 wavenumbers include 1234  $\text{cm}^{-1}$  [asymmetric  $\text{PO}_2^-$  (Nucleic acid)], 1319  $\text{cm}^{-1}$  (Amide  
343 III), 1416  $\text{cm}^{-1}$  (proteins), 1497  $\text{cm}^{-1}$  (Amide II), 1616  $\text{cm}^{-1}$  (Amide I), 1667  $\text{cm}^{-1}$   
344 (Amide I  $\beta$ -turns of proteins), 2893  $\text{cm}^{-1}$  ( $\text{CH}_3$  symmetric stretching) and 3078  $\text{cm}^{-1}$   
345 (Amide B, Stretching C-H). Furthermore, we observed a great variability in the peak  
346 absorbance at various IR wavenumbers mentioned above for each NP treatment  
347 within 35-day-old class and for 100 mg/kg NP exposure within 21- or 50-day-old  
348 classes (see ESI Figure S8), which suggests the effects of NP varied with different  
349 age stages.

350 To further explore the potential toxic effects of NP on testicular cell functions,  
351 the IR absorbance ratios were calculated, which can be used to describe the structural

352 and compositional changes in biomolecules. As shown in **Figure 3A**, the  
353 lipid-to-protein ratios of high-dose (50 mg/kg and 100 mg/kg) NP exposures are much  
354 higher than those of the control within the 50-day-old class but much lower within  
355 both 21- and 35-day-old classes ( $P<0.01$ ). In case of the peptide aggregation (**Figure**  
356 **3B**), remarked decreases were found in 50 mg/kg and 100 mg/kg NP exposure for 21-,  
357 35- and 50-day-old rats ( $P<0.05$ ). The 50 mg/kg and 100 mg/kg NP-treated rats show  
358 a significant decrease in the ratios of Amide I-to-Amide II compared to the control  
359 rats within 21- and 35-day-old classes ( $P<0.001$ ), but the 50-day-old class show no  
360 obvious differences among all NP treatments in this respect ( $P>0.05$ ) (**Figure 3C**).  
361 The 50 mg/kg and 100 mg/kg NP treatments in 21- and 35-day-old rats exhibit much  
362 lower ratios of phosphate-to-carbohydrate in comparison with the control ( $P<0.001$ ),  
363 except the 50-day-old rats (**Figure 3D**). In addition, we reveal a significant interaction  
364 between NP concentrations and age classes that influence these parameters (two-way  
365 ANOVA,  $P_{interaction}<0.001$ ) (see **ESI Figure S9**). Also, the exposure life-stage was an  
366 independent factor affecting NP-induced biomolecular alterations in testicular cells  
367 (effect of ages  $P<0.01$ ).

### 368 **3.3 Raman spectroscopy detects biomolecular alterations in testicular interstitial** 369 **tissues of NP-exposed rats**

370 Herein, Raman spectra of testicular interstitial tissue were recorded in the spectral  
371 region from 1800-900  $\text{cm}^{-1}$  (see **ESI Figure S10**). By performing PCA-LDA model  
372 for classification, we are able to visualize clear segregation among different  
373 NP-treatment categories of all age-classes (**Figure 4A-C**). Meanwhile, the main  
374 absorption variations between NP-treated and control groups within each age-class  
375 were observed by applying between-class covariance matrix (see **ESI Figure S11**),  
376 reflecting NP-induced biomolecular alterations in testicular interstitial cells. Along  
377 LD1 dimension, testicular interstitial tissue of differently aged NP-treated rats  
378 segregate away from the control, and these differences are statistically significant for  
379 all age-classes ( $P<0.001$ ) (**Figure 4D-F**). There is a significant main effect of NP  
380 treatment, exposure age, and interaction between these two factors on differences in



381 LD1 value compared with control group (two-way ANOVA, all  $P < 0.001$ ) (see ESI  
382 **Figure S12**).

383 Cluster vectors plots derived from the LD1 space denotes where the differences  
384 between NP-treated and control categories of 21-day-old rats are apparent, with  
385 prominent Raman wavenumbers at  $997\text{ cm}^{-1}$  (phospholipids, glucose-I-phosphate),  
386  $1007\text{ cm}^{-1}$  (phenylalanine, carbamide),  $1131\text{ cm}^{-1}$  (palmitic acid, fatty acid, C-C  
387 skeletal stretching),  $1200\text{ cm}^{-1}$  (nucleic acids, phosphates),  $1296\text{ cm}^{-1}$  (fatty acids),  
388  $1465\text{ cm}^{-1}$  (lipids),  $1650\text{ cm}^{-1}$  (C=C=C bonds in unsaturated fatty acids of  
389 phospholipids) and  $1675\text{ cm}^{-1}$  (Amide I) (**Figure 4G**). From the cluster vectors plot of  
390 the 35-day-old class (**Figure 4H**), there are highlighted peaks at  $918\text{ cm}^{-1}$  (glycogen,  
391 lactic acid),  $997\text{ cm}^{-1}$  (phospholipids, glucose-I-phosphate),  $1007\text{ cm}^{-1}$  (phenylalanine,  
392 carbamide),  $1200\text{ cm}^{-1}$  (nucleic acids, phosphates),  $1346\text{ cm}^{-1}$  (Amide III vibrations of  
393 protein and CH deformation of protein and lipid),  $1465\text{ cm}^{-1}$  (lipids), as well as the  
394 peak associated with Amide I ( $1647$  and  $1689\text{ cm}^{-1}$ ). As depicted for the 50-day-old  
395 group in **Figure 4I**, distinguishing wavenumbers include  $1090\text{ cm}^{-1}$  (lipids),  $1142$   
396  $\text{cm}^{-1}$  (Sphingomyelin),  $1184\text{ cm}^{-1}$  [DNA (cytosine, guanine and adenine)],  $1307\text{ cm}^{-1}$   
397 ( $\text{CH}_3/\text{CH}_2$  twisting or bending mode of lipid/collagen),  $1334\text{ cm}^{-1}$  (DNA),  $1402\text{ cm}^{-1}$   
398 (collagen, the  $\text{CH}_3$  symmetric deformation vibrations),  $1485\text{ cm}^{-1}$  (nucleotide acid  
399 purine bases), and  $1584\text{ cm}^{-1}$  [pyrimidine ring (nucleic acids), heme protein/C=C  
400 phenylalanine]. In addition, there is a significant difference in the peak absorbance of  
401 above-mentioned Raman wavenumbers between NP-treated and control groups at  
402 different age-classes (see ESI **Figure S13**).

403 In addition, the ratio of protein-to-lipid significantly changed in each  
404 NP-treatment vs. control for all age-classes ( $P < 0.05$ ), except 50 mg/kg NP exposure  
405 for 35-day-old rats (**Figure 5A**). In the case of unsaturated lipids level, only 50 mg/kg  
406 NP exposure for 35- and 50-day-old rats exhibit no statistical differences in  
407 comparison to the corresponding control ( $P > 0.05$ ) (**Figure 5B**). As shown in **Figure**  
408 **5C**, the saturated lipids levels of the 50 mg/kg and 100 mg/kg NP groups are much  
409 higher than the control group within the 21-day-old class but much lower within both

410 35- and 50-day-old classes ( $P<0.05$ ). Two way ANOVA reveals the main significant  
411 effects of age, NP treatment and a significant interaction between both factors for  
412 these ratios change ( $P<0.001$ ) (see ESI Figure S14).

### 413 **3.4 Impact of NP on cell viability in Sertoli cells**

414 The CCK-8 assay reveals that exposure of SCs to NP (2.5-20  $\mu\text{M}$ ) reduced cell  
415 viability in a dose- and time-dependent manner (see ESI Figure S15). In particular,  
416 SCs treated with 10 and 20  $\mu\text{M}$  NP exhibited significantly decreased cell viability  
417 when compared with control (0  $\mu\text{M}$  NP), respectively, after incubation for 12 h and 24  
418 h ( $P<0.05$ ). In subsequent experiments, we chose 12 h as the end timepoint for  
419 ATR-FITR spectral measurements.

### 420 **3.5 ATR-FITR spectroscopy detects biochemical changes in NP-treated Sertoli** 421 **cells (SCs) in vitro**

422 The IR spectral regions we investigated are the biochemical-cell fingerprint region  
423 ( $1800\text{-}900\text{ cm}^{-1}$ ) and the lipid region ( $3200\text{-}2800\text{ cm}^{-1}$ ) (see ESI Figure S16). Five  
424 clusters for 0, 2.5, 5, 10 and 20  $\mu\text{M}$  NP-treated SCs are well delineated on each 2D  
425 PCA-LDA scores plot [LD1 vs. Linear discriminant 2 (LD2)], showing clear cluster  
426 separations, with no overlap of the 20  $\mu\text{M}$  NP-treatment with the control group in the  
427  $1800\text{-}900\text{ cm}^{-1}$  region (Figure 6A), but total overlap of the 2.5  $\mu\text{M}$  NP-treatment with  
428 the control group in the  $3200\text{-}2800\text{ cm}^{-1}$  region (Figure 6B). As shown in Figure  
429 6C-D, NP-induced effects observed in LD1 space exhibit significant differences  
430 between each NP-treatment and the control groups in both  $1800\text{-}900\text{ cm}^{-1}$  and  
431  $3200\text{-}2800\text{ cm}^{-1}$  regions ( $P<0.001$ ). Interestingly, the dose-response of SCs treated  
432 with increasing concentrations of NP is nonlinear and varies markedly between these  
433 two regions.

434 Cluster vectors after PCA-LDA derived from the targeted regions to identify  
435 wavenumbers segregating control SCs from NP-treated SCs categories are depicted in  
436 Figure 6E-F. The fingerprint region shows prominent peaks at  $999\text{ cm}^{-1}$  (C-C  
437 stretching of DNA),  $1535\text{ cm}^{-1}$  (Amide II),  $1605\text{ cm}^{-1}$  [DNA,  $\delta(\text{NH}_2)$ ] and  $1708\text{ cm}^{-1}$

438 (A-DNA base pairing vibration) (**Figure 6E**); statistical significances for absorbance  
439 values of these wavenumbers are observed only between 20  $\mu\text{M}$  NP-treated and  
440 control SCs (see **ESI Figure S17**). The lipid region generated distinguishing peaks at  
441  $2821\text{ cm}^{-1}$  (stretching C-H),  $2975\text{ cm}^{-1}$  (stretching N-H, stretching C-H),  $3015\text{ cm}^{-1}$   
442 [ $\nu(\text{=CH})$  of lipids] and  $3050\text{ cm}^{-1}$  [Amid B (N-H stretching)] (**Figure 6F**), and there  
443 are significant differences in absorbance of these wavenumbers between NP-treated  
444 and control groups, except for 10  $\mu\text{M}$  NP-treated SCs (see **ESI Figure S17**). Notably,  
445 these band variations correlate well with the spatial distribution patterns observed  
446 using between-class covariance matrix (see **ESI Figure S18**). As shown in **Figure 7**,  
447 SCs treated with 10  $\mu\text{M}$  or 20  $\mu\text{M}$  NP exhibit much higher lipid-to-protein ratios and  
448 much lower peptide aggregation levels than the control SCs ( $P<0.01$ ). In addition, NP  
449 induced significant decreases of Amide I-to-Amide II ratio and  
450 phosphate-to-carbohydrate ratio in comparison to control SCs ( $P<0.01$ ).

#### 451 **4. Discussion**

452 The primary aim of the present study was to apply ATR-FTIR and Raman  
453 spectroscopy to monitor the testicular biomolecular changes induced by exposure of  
454 male rats aged 21, 35 or 50 days to NP. While IR spectra obtained from testicular cells  
455 or SCs can be used to distinguish between the control *vs.* NP-treated groups, by  
456 employing Raman spectroscopy to analyse the interstitial tissue, clear differences  
457 between treated and untreated animals are observed, supporting the notion that NP  
458 exposure results in testicular toxicity. The results obtained by means of  
459 spectrochemical investigations highlight the major differences in the peak intensities  
460 assigned to proteins, lipids and nucleic acids that may be responsible for some of the  
461 NP-induced effects on spermatogenesis. In addition, an age  $\times$  NP treatment interaction  
462 was also detected for LD1 score and intensity ratios of the main spectral components.

463 A balance of the metabolism of lipid and protein in testicular cells is crucial for  
464 normal spermatogenesis and membrane remodelling in developing germ cells. Herein,  
465 successful differentiation in the fingerprint and lipid C-H regions (**Figure 1A-B and**  
466 **6A-B**) confirm effects of NP on *in vivo* testis and *in vitro* primary SCs. Moreover,

467 profound differences are observed in spectral peaks assigned to fatty acids/lipids and  
468 amide in proteins. Fatty acids and amide absorptions are mainly associated with the  
469 outer cell membrane, and the large spectral alterations associated with lipid content  
470 and conformational protein alterations could point to the disruption of the cell  
471 membrane structure and integrity (Strong et al., 2016). The lipid/protein ratio was  
472 frequently used to identify molecular and compositional changes within tissues.  
473 Significant alterations are observed in the lipid-to-protein ratio for the NP-treated  
474 samples (**Figure 3A and 7A**), indicating an alteration in the cellular lipid and protein  
475 metabolism caused by NP exposure (Yonar et al., 2018). These biomolecular  
476 alterations, in turn, may be related to NP-induced apoptosis or dysfunction of SCs and  
477 germ cells that lead to seminiferous tubule degeneration with impaired  
478 spermatogenesis.

479 The alterations of protein-secondary structure inside the targeted cells have been  
480 identified as the cause of cell death, either by necrosis or apoptosis (Yousef et al.,  
481 2016). The Amide I and II bands are the most prominent vibrational bands of the  
482 protein backbone and a sensitive indicator of conformational changes of secondary  
483 structure of proteins. The Amide I-to-Amide II ratio describes variation in the overall  
484 molecular structures of proteins. In our study, the characteristic bands for Amide I,  
485 Amide II, and Amide III are clearly observed. Simultaneously, the values of Amide  
486 I-to-Amide II ratios are remarkably decreased for NP-treated SCs and rats aged 21 or  
487 35 days, compared to the control (**Figure 3C and 7C**). These findings, which suggest  
488 protein conformational changes in testicular cells and SCs after exposed to NP, are  
489 also consistent with those of other studies showing that NP is able to induce apoptosis  
490 in testicular cells *in vivo* and in SCs *in vitro* (Wu et al., 2009; Duan et al., 2016a;  
491 Duan et al., 2016b; Huang et al., 2016). The modifications of Amide I and II could  
492 predict the occurrence of protein aggregation from protein oxidation (Xin et al., 2017).  
493 We observed marked decreases in protein aggregation in testicular cells and SCs in  
494 response to NP treatment (**Figure 3B and 7B**). Indeed, exposure to NP induces  
495 oxidative stress in testicular tissue and SCs, and alters the activity levels of

496 antioxidative enzymes (Duan et al., 2016a; Duan et al., 2016b). Here we suggest that  
497 NP exposure is capable of inducing oxidative protein damage, which if not removed,  
498 could accumulate over time and cause deterioration of testicular cell function.

499       Some studies confirm that NP exposure could alter the enzymes of carbohydrate  
500 metabolism and negatively impact carbohydrate metabolism in the animal's liver  
501 (Jubendradass et al., 2012; Yang et al., 2017). Phosphate serves as a transmitter of  
502 biological signals and plays a central role in increasing the turnover rates of cellular  
503 enzymes (Cassago et al., 2012). Accordingly, we calculated the intensity ratio of  
504 phosphate-to-carbohydrate which serves as a potential biomarker to identify metabolic  
505 changes (Theophilou et al., 2016; Paraskevaidi et al., 2017a). Prominently, NP  
506 exposure provoked decreases of phosphate-to-carbohydrate ratio in testicular cells  
507 from rats of 21- or 35-days-old classes and in primary SCs (**Figure 3D and 7D**). The  
508 crucial roles of AMPK/Akt in the regulation of cellular metabolism have been well  
509 documented (Mihaylova and Shaw, 2011; Yu and Cui, 2016). Moreover, NP-induced  
510 changes in AMPK/Akt-mediated pathways possibly contribute to testicular toxicity  
511 and spermatogenesis impairment (Huang et al., 2016; Duan et al., 2017b; Su et al.,  
512 2018). In the light of these observations, we propose that NP exposure alters the  
513 metabolic programming of the cell fate by regulating signalling molecules important  
514 for testicular development.

515       Between the seminiferous tubules lies the interstitial tissue, a loose connective  
516 tissue mainly containing the steroidogenic Leydig cells. The Leydig cells produce  
517 testosterone, which in turn stimulates SCs to secrete a wide variety of factors required  
518 for the proliferation and differentiation of germ cells. Treatment with NP resulted in  
519 decreases in serum testosterone levels in male rats (Aly et al., 2012; Huang et al.,  
520 2016; Duan et al., 2017a), which was probably caused by Leydig cell dysfunction.  
521 Raman spectroscopy was successfully employed to interrogate the testis interstitium  
522 in this study. Our results show that NP exposure generated a range of biomolecular  
523 alterations related to structural proteins and lipids/fatty acids. Also, results highlight  
524 marked variations in the ratio of lipid-to-protein and the levels of unsaturated lipids

525 and saturated lipids in response to NP treatment (**Figure 5**). There are abundant lipid  
526 droplets visible in the cytoplasm of immature Leydig cells. Leydig cell lipid droplets  
527 primarily contain cholesterol esters; this cholesterol is the major source of cholesterol  
528 for androgen biosynthesis (Ma et al., 2018). Possibly, NP alters essential constituents  
529 of cell membranes resulting in Leydig cell injury, subsequently damaging the cellular  
530 biomolecules such as functional lipids. One of the effects observed in our experiments  
531 with NP treatments was the alterations in bands related to phospholipids.  
532 Phospholipids have been implicated in metabolic events associated with cell structure  
533 and function (Yang et al., 2012). From these findings, we conclude that NP exposure  
534 appears to act as a lipid metabolism disrupter, inducing deleterious effects in Leydig  
535 cells *via* metabolic perturbations and membrane disruption, and therefore, resulting in  
536 decreased output of testosterone and adversely influencing spermatogenesis.

537 In this work, both IR and Raman spectra indicate that NP can induce alterations  
538 in DNA/RNA. Particularly, the observed modifications in the pattern of DNA could  
539 suggest a genotoxic effect of NP in SCs and Leydig cells. Recently, NP has been  
540 reported to induce genotoxicity by inducing hepatic DNA fragmentation or DNA  
541 damage in different organs of *C. punctatus* (Sharma and Chadha, 2017; Sayed and  
542 Soliman, 2018). DNA damage, which could result in genome instability and apoptosis,  
543 could be a consequence of oxidative stress. At the cellular level, NP may stimulate the  
544 formation of reactive oxygen species, resulting in oxidative stress (Gong and Han,  
545 2006; Duan et al., 2016b). Based on this evidence, we demonstrate that NP may  
546 interfere with cellular metabolism, and this effect coincides with potential DNA  
547 damage in testicular cells although the exact mechanism remains unknown.

548 The proportion and the differentiation (immature and mature cells) state of each  
549 cell population in the testis varies considerably between the 21-, 35- and 50-day-old  
550 rats. From our results of two-way ANOVA analysis, we identify a number of  
551 biomolecular parameters that are altered by the age  $\times$  treatment statistical interaction  
552 (**Figure S7, 9, 12 and 14**). These interaction effects indicate that the status of  
553 testicular cell metabolism (growth, maintenance, and biomolecular composition)

554 affects downstream cell signalling events in response to NP exposure, and the  
555 exposure life-stage likely exerts independent effects on spectral features of testicular  
556 cells. Specifically, the Raman results show that the 21- or 35-day-old rats responded  
557 to the NP treatment highlighting the same bands at 997  $\text{cm}^{-1}$ , 1007  $\text{cm}^{-1}$ , 1200  $\text{cm}^{-1}$   
558 and 1465  $\text{cm}^{-1}$  although with different intensities (**Figure 4G-H**). However, the rats at  
559 the three ages share no common spectral peaks in response to NP exposure. Moreover,  
560 the peaks corresponding to lipids/fatty acids responses of 21-day-old NP-treated rats  
561 are much more extensive than those of the 35- or 50-day-old rats treated with NP.  
562 Differences among three age classes can be ascribed to testicular cells at different  
563 development stages that exhibit alterations in biomolecular components and properties,  
564 resulting in different spectral characteristics induced by the same NP treatment.

## 565 **5. Conclusions**

566 Testicular biomolecular alterations in the intensity of spectral bands following NP  
567 treatment indicate effects on cellular metabolism and membrane integrity. ATR-FTIR  
568 and Raman spectroscopy are complementary vibrational spectrochemical techniques,  
569 which allow the discrimination and quantitative characterization of different peaks  
570 and targeted areas between NP-treated and untreated rats at different ages.  
571 Biomolecular differences were noted after NP administration in rats: proteins (1416  
572  $\text{cm}^{-1}$ ), Amide I (1667, 1670  $\text{cm}^{-1}$ ), Amide II (1582, 1504, 1497  $\text{cm}^{-1}$ ), fatty acids (1732  
573  $\text{cm}^{-1}$ ), RNA (1111  $\text{cm}^{-1}$ ) in IR spectra from testicular cells; and lipids (1465  $\text{cm}^{-1}$ ),  
574 phospholipids (1650, 997  $\text{cm}^{-1}$ ), nucleic acid bands (1485, 1200  $\text{cm}^{-1}$ ), phenylalanine  
575 (1007  $\text{cm}^{-1}$ ), DNA (1334, 1184  $\text{cm}^{-1}$ ) in Raman spectra from interstitial tissue.  
576 Intriguingly, NP has different effects on testicular cellular components depending on  
577 the age of the animal at the time of exposure. Moreover, we observed NP-induced  
578 spectral changes in SCs, which are mainly assigned to Amide II, DNA and lipid CH  
579 stretching. This study could be the basis for future investigations lending new insights  
580 into our understanding of the mechanisms of NP-induced testicular toxicity in rats.

581

## 582 **Acknowledgements**

583 This work was supported by the China Postdoctoral Science Foundation (nos.  
584 2016M602310) and the Doctoral Startup Project of Hubei University of Medicine  
585 (nos. 2017QDJZR07).

586

587 **Conflict of interest**

588 The authors declare that there are no conflicts of interest.

589



590 **Reference**

- 591 Aly, H.A., Domenech, O., Banjar, Z.M., 2012. Effect of nonylphenol on male reproduction: analysis of  
592 rat epididymal biochemical markers and antioxidant defense enzymes. *Toxicology and Applied*  
593 *Pharmacology* 261, 134-141.
- 594 Andrew Chan, K.L., Kazarian, S.G., 2016. Attenuated total reflection Fourier-transform infrared  
595 (ATR-FTIR) imaging of tissues and live cells. *Chemical Society reviews* 45, 1850-1864.
- 596 Aparicio, I., Martin, J., Abril, C., Santos, J.L., Alonso, E., 2017. Determination of household and  
597 industrial chemicals, personal care products and hormones in leafy and root vegetables by liquid  
598 chromatography-tandem mass spectrometry. *Journal of chromatography. A*.
- 599 Asimakopoulos, A.G., Thomaidis, N.S., Koupparis, M.A., 2012. Recent trends in biomonitoring of  
600 bisphenol A, 4-t-octylphenol, and 4-nonylphenol. *Toxicology letters* 210, 141-154.
- 601 Baker, M.J., Trevisan, J., Bassan, P., Bhargava, R., Butler, H.J., Dorling, K.M., Fielden, P.R., Fogarty, S.W.,  
602 Fullwood, N.J., Heys, K.A., Hughes, C., Lasch, P., Martin-Hirsch, P.L., Obinaju, B., Sockalingum, G.D.,  
603 Sule-Suso, J., Strong, R.J., Walsh, M.J., Wood, B.R., Gardner, P., Martin, F.L., 2014. Using Fourier  
604 transform IR spectroscopy to analyze biological materials. *Nat Protoc* 9, 1771-1791.
- 605 Butler, H.J., Ashton, L., Bird, B., Cinque, G., Curtis, K., Dorney, J., Esmonde-White, K., Fullwood, N.J.,  
606 Gardner, B., Martin-Hirsch, P.L., Walsh, M.J., McAinsh, M.R., Stone, N., Martin, F.L., 2016. Using Raman  
607 spectroscopy to characterize biological materials. *Nature protocols* 11, 664-687.
- 608 Cassago, A., Ferreira, A.P., Ferreira, I.M., Fornezari, C., Gomes, E.R., Greene, K.S., Pereira, H.M., Garratt,  
609 R.C., Dias, S.M., Ambrosio, A.L., 2012. Mitochondrial localization and structure-based phosphate  
610 activation mechanism of Glutaminase C with implications for cancer metabolism. *Proceedings of the*  
611 *National Academy of Sciences of the United States of America* 109, 1092-1097.
- 612 Chapin, R.E., Delaney, J., Wang, Y., Lanning, L., Davis, B., Collins, B., Mintz, N., Wolfe, G., 1999. The  
613 effects of 4-nonylphenol in rats: a multigeneration reproduction study. *Toxicological sciences : an*  
614 *official journal of the Society of Toxicology* 52, 80-91.
- 615 Chen, J., Xiao, H.J., Qi, T., Chen, D.L., Long, H.M., Liu, S.H., 2015. Rare earths exposure and male  
616 infertility: the injury mechanism study of rare earths on male mice and human sperm. *Environmental*  
617 *science and pollution research international* 22, 2076-2086.
- 618 Cheng, Y., Shan, Z., Zhou, J., Bu, Y., Li, P., Lu, S., 2017. Effects of 4-nonylphenol in drinking water on the  
619 reproductive capacity of Japanese quails (*Coturnix japonica*). *Chemosphere* 175, 219-227.
- 620 Deng, P., Zhong, D., Nan, F., Liu, S., Li, D., Yuan, T., Chen, X., Zheng, J., 2010. Evidence for the  
621 bioactivation of 4-nonylphenol to quinone methide and ortho-benzoquinone metabolites in human  
622 liver microsomes. *Chemical research in toxicology* 23, 1617-1628.
- 623 Diao, P., Chen, Q., Wang, R., Sun, D., Cai, Z., Wu, H., Duan, S., 2017. Phenolic endocrine-disrupting  
624 compounds in the Pearl River Estuary: Occurrence, bioaccumulation and risk assessment. *The Science*  
625 *of the total environment* 584-585, 1100-1107.
- 626 Duan, P., Hu, C., Butler, H.J., Quan, C., Chen, W., Huang, W., Tang, S., Zhou, W., Yuan, M., Shi, Y., Martin,  
627 F.L., Yang, K., 2016a. Effects of 4-nonylphenol on spermatogenesis and induction of testicular  
628 apoptosis through oxidative stress-related pathways. *Reproductive toxicology* 62, 27-38.
- 629 Duan, P., Hu, C., Butler, H.J., Quan, C., Chen, W., Huang, W., Tang, S., Zhou, W., Yuan, M., Shi, Y., Martin,  
630 F.L., Yang, K., 2017a. 4-Nonylphenol induces disruption of spermatogenesis associated with oxidative  
631 stress-related apoptosis by targeting p53-Bcl-2/Bax-Fas/FasL signaling. *Environmental toxicology* 32,  
632 739-753.

633 Duan, P., Hu, C., Quan, C., Yu, T., Huang, W., Chen, W., Tang, S., Shi, Y., Martin, F.L., Yang, K., 2017b.  
634 4-Nonylphenol induces autophagy and attenuates mTOR-p70S6K/4EBP1 signaling by modulating  
635 AMPK activation in Sertoli cells. *Toxicol Lett* 267, 21-31.

636 Duan, P., Hu, C., Quan, C., Yu, T., Zhou, W., Yuan, M., Shi, Y., Yang, K., 2016b. 4-Nonylphenol induces  
637 apoptosis, autophagy and necrosis in Sertoli cells: Involvement of ROS-mediated AMPK/AKT-mTOR  
638 and JNK pathways. *Toxicology* 341-343, 28-40.

639 Eberhardt, K., Stiebing, C., Matthaus, C., Schmitt, M., Popp, J., 2015. Advantages and limitations of  
640 Raman spectroscopy for molecular diagnostics: an update. *Expert review of molecular diagnostics* 15,  
641 773-787.

642 El-Sayed Ali, T., Abdel-Aziz, S.H., El-Sayed, A.F., Zeid, S., 2014. Structural and functional effects of early  
643 exposure to 4-nonylphenol on gonadal development of Nile tilapia (*Oreochromis niloticus*):  
644 a-histological alterations in ovaries. *Fish physiology and biochemistry* 40, 1509-1519.

645 Fairbairn, D.J., Karpuzcu, M.E., Arnold, W.A., Barber, B.L., Kaufenberg, E.F., Koskinen, W.C., Novak, P.J.,  
646 Rice, P.J., Swackhamer, D.L., 2016. Sources and transport of contaminants of emerging concern: A  
647 two-year study of occurrence and spatiotemporal variation in a mixed land use watershed. *The*  
648 *Science of the total environment* 551-552, 605-613.

649 Gajjar, K., Heppenstall, L.D., Pang, W., Ashton, K.M., Trevisan, J., Patel, II, Llabjani, V., Stringfellow, H.F.,  
650 Martin-Hirsch, P.L., Dawson, T., Martin, F.L., 2012. Diagnostic segregation of human brain tumours  
651 using Fourier-transform infrared and/or Raman spectroscopy coupled with discriminant analysis.  
652 *Analytical methods : advancing methods and applications* 5, 89-102.

653 Gong, Y., Han, X.D., 2006. Nonylphenol-induced oxidative stress and cytotoxicity in testicular Sertoli  
654 cells. *Reproductive toxicology* 22, 623-630.

655 Heppenstall, L.D., Strong, R.J., Trevisan, J., Martin, F.L., 2013. Incorporation of deuterium oxide in  
656 MCF-7 cells to shed further mechanistic insights into benzo[a]pyrene-induced low-dose effects  
657 discriminated by ATR-FTIR spectroscopy. *The Analyst* 138, 2583-2591.

658 Huang, W., Quan, C., Duan, P., Tang, S., Chen, W., Yang, K., 2016. Nonylphenol induced apoptosis and  
659 autophagy involving the Akt/mTOR pathway in prepubertal Sprague-Dawley male rats in vivo and in  
660 vitro. *Toxicology* 373, 41-53.

661 Iqbal, M., Bhatti, I.A., 2015. Gamma radiation/H<sub>2</sub>O<sub>2</sub> treatment of a nonylphenol ethoxylates:  
662 Degradation, cytotoxicity, and mutagenicity evaluation. *Journal of hazardous materials* 299, 351-360.

663 Jambor, T., Tvrda, E., Tusimova, E., Kovacik, A., Bistakova, J., Forgacs, Z., Lukac, N., 2017. In vitro effect  
664 of 4-nonylphenol on human chorionic gonadotropin (hCG) stimulated hormone secretion, cell viability  
665 and reactive oxygen species generation in mice Leydig cells. *Environmental pollution* 222, 219-225.

666 Jin, N., Paraskevaidi, M., Semple, K.T., Martin, F.L., Zhang, D., 2017. Infrared Spectroscopy Coupled with  
667 a Dispersion Model for Quantifying the Real-Time Dynamics of Kanamycin Resistance in Artificial  
668 Microbiota. *Analytical chemistry* 89, 9814-9821.

669 Jubendradass, R., D'Cruz, S.C., Mathur, P.P., 2012. Long-term exposure to nonylphenol affects insulin  
670 signaling in the liver of adult male rats. *Human & experimental toxicology* 31, 868-876.

671 Lee, H.R., Jeung, E.B., Cho, M.H., Kim, T.H., Leung, P.C., Choi, K.C., 2013. Molecular mechanism(s) of  
672 endocrine-disrupting chemicals and their potent oestrogenicity in diverse cells and tissues that  
673 express oestrogen receptors. *Journal of cellular and molecular medicine* 17, 1-11.

674 Li, H., Martin, F.L., Zhang, D., 2017. Quantification of Chemotaxis-Related Alkane Accumulation in  
675 *Acinetobacter baylyi* Using Raman Microspectroscopy. *Analytical chemistry* 89, 3909-3918.

676 Li, J., Strong, R., Trevisan, J., Fogarty, S.W., Fullwood, N.J., Jones, K.C., Martin, F.L., 2013a. Dose-related

677 alterations of carbon nanoparticles in mammalian cells detected using biospectroscopy: potential for  
678 real-world effects. *Environmental science & technology* 47, 10005-10011.

679 Li, J., Tian, M., Cui, L., Dwyer, J., Fullwood, N.J., Shen, H., Martin, F.L., 2016. Low-dose carbon-based  
680 nanoparticle-induced effects in A549 lung cells determined by biospectroscopy are associated with  
681 increases in genomic methylation. *Scientific reports* 6, 20207.

682 Li, J., Ying, G.G., Jones, K.C., Martin, F.L., 2015. Real-world carbon nanoparticle exposures induce brain  
683 and gonadal alterations in zebrafish (*Danio rerio*) as determined by biospectroscopy techniques. *The*  
684 *Analyst* 140, 2687-2695.

685 Li, X., Ying, G.G., Zhao, J.L., Chen, Z.F., Lai, H.J., Su, H.C., 2013b. 4-Nonylphenol, bisphenol-A and  
686 triclosan levels in human urine of children and students in China, and the effects of drinking these  
687 bottled materials on the levels. *Environment international* 52, 81-86.

688 Lima, K.M., Gajjar, K.B., Martin-Hirsch, P.L., Martin, F.L., 2015. Segregation of ovarian cancer stage  
689 exploiting spectral biomarkers derived from blood plasma or serum analysis: ATR-FTIR spectroscopy  
690 coupled with variable selection methods. *Biotechnology progress* 31, 832-839.

691 Lin, C.C., Chien, C.J., Tsai, M.S., Hsieh, C.J., Hsieh, W.S., Chen, P.C., 2017. Prenatal phenolic compounds  
692 exposure and neurobehavioral development at 2 and 7 years of age. *The Science of the total*  
693 *environment* 605-606, 801-810.

694 Liu, X., Nie, S., Chen, Y., Huang, D., Xie, M., 2014. Effects of 4-nonylphenol isomers on cell receptors  
695 and mitogen-activated protein kinase pathway in mouse Sertoli TM4 cells. *Toxicology* 326, 1-8.

696 Lu, Y., Luo, B., Li, J., Dai, J.Y., 2016. Perfluorooctanoic acid disrupts the blood-testis barrier and  
697 activates the TNF alpha/p38 MAPK signaling pathway in vivo and in vitro. *Arch Toxicol* 90, 971-983.

698 Ma, Y., Zhou, Y., Zhu, Y.C., Wang, S.Q., Ping, P., Chen, X.F., 2018. Lipophagy Contributes to Testosterone  
699 Biosynthesis in Male Rat Leydig Cells. *Endocrinology* 159, 1119-1129.

700 Mihaylova, M.M., Shaw, R.J., 2011. The AMPK signalling pathway coordinates cell growth, autophagy  
701 and metabolism. *Nature cell biology* 13, 1016-1023.

702 Noorimotlagh, Z., Haghghi, N.J., Ahmadi Moghadam, M., Rahim, F., 2017. An updated systematic  
703 review on the possible effect of nonylphenol on male fertility. *Environmental science and pollution*  
704 *research international* 24, 3298-3314.

705 Obinaju, B.E., Fullwood, N.J., Martin, F.L., 2015. Distinguishing nuclei-specific benzo[a]pyrene-induced  
706 effects from whole-cell alterations in MCF-7 cells using Fourier-transform infrared spectroscopy.  
707 *Toxicology* 335, 27-34.

708 Obinaju, B.E., Martin, F.L., 2016. ATR-FTIR spectroscopy reveals polycyclic aromatic hydrocarbon  
709 contamination despite relatively pristine site characteristics: Results of a field study in the Niger Delta.  
710 *Environment international* 89-90, 93-101.

711 Owens, G.L., Gajjar, K., Trevisan, J., Fogarty, S.W., Taylor, S.E., Da Gama-Rose, B., Martin-Hirsch, P.L.,  
712 Martin, F.L., 2014. Vibrational biospectroscopy coupled with multivariate analysis extracts potentially  
713 diagnostic features in blood plasma/serum of ovarian cancer patients. *Journal of biophotonics* 7,  
714 200-209.

715 Paraskevaïdi, M., Morais, C.L.M., Lima, K.M.G., Snowden, J.S., Saxon, J.A., Richardson, A.M.T., Jones, M.,  
716 Mann, D.M.A., Allsop, D., Martin-Hirsch, P.L., Martin, F.L., 2017a. Differential diagnosis of Alzheimer's  
717 disease using spectrochemical analysis of blood. *Proceedings of the National Academy of Sciences of*  
718 *the United States of America* 114, E7929-E7938.

719 Paraskevaïdi, M., Morais, C.L.M., Lima, K.M.G., Snowden, J.S., Saxon, J.A., Richardson, A.M.T., Jones, M.,  
720 Mann, D.M.A., Allsop, D., Martin-Hirsch, P.L., Martin, F.L., 2017b. Differential diagnosis of Alzheimer's

721 disease using spectrochemical analysis of blood. *Proceedings of the National Academy of Sciences of*  
722 *the United States of America* 114, E7929-E7938.

723 Pastor-Belda, M., Vinas, P., Campillo, N., Hernandez-Cordoba, M., 2017. Magnetic solid phase  
724 extraction with CoFe<sub>2</sub>O<sub>4</sub>/oleic acid nanoparticles coupled to gas chromatography-mass spectrometry  
725 for the determination of alkylphenols in baby foods. *Food chemistry* 221, 76-81.

726 Peng, F.J., Pan, C.G., Zhang, M., Zhang, N.S., Windfeld, R., Salvito, D., Selck, H., Van den Brink, P.J., Ying,  
727 G.G., 2017. Occurrence and ecological risk assessment of emerging organic chemicals in urban rivers:  
728 Guangzhou as a case study in China. *The Science of the total environment* 589, 46-55.

729 Riding, M.J., Martin, F.L., Trevisan, J., Llabjani, V., Patel, I., Jones, K.C., Semple, K.T., 2012.  
730 Concentration-dependent effects of carbon nanoparticles in gram-negative bacteria determined by  
731 infrared spectroscopy with multivariate analysis. *Environmental pollution* 163, 226-234.

732 Sayed, A.E.H., Soliman, H.A.M., 2018. Modulatory effects of green tea extract against the hepatotoxic  
733 effects of 4-nonylphenol in catfish (*Clarias gariepinus*). *Ecotoxicology and environmental safety* 149,  
734 159-165.

735 Sharma, M., Chadha, P., 2017. Widely used non-ionic surfactant 4-nonylphenol: showing genotoxic  
736 effects in various tissues of *Channa punctatus*. *Environmental science and pollution research*  
737 *international* 24, 11331-11339.

738 Soares, A., Guieysse, B., Jefferson, B., Cartmell, E., Lester, J.N., 2008. Nonylphenol in the environment:  
739 a critical review on occurrence, fate, toxicity and treatment in wastewaters. *Environment international*  
740 34, 1033-1049.

741 Staniszewska, M., Nehring, I., Mudrak-Cegiolka, S., 2016. Changes of concentrations and possibility of  
742 accumulation of bisphenol A and alkylphenols, depending on biomass and composition, in  
743 zooplankton of the Southern Baltic (Gulf of Gdansk). *Environmental pollution* 213, 489-501.

744 Strong, R.J., Halsall, C.J., Jones, K.C., Shore, R.F., Martin, F.L., 2016. Infrared spectroscopy detects  
745 changes in an amphibian cell line induced by fungicides: Comparison of single and mixture effects.  
746 *Aquatic toxicology* 178, 8-18.

747 Su, Y., Quan, C., Li, X., Shi, Y., Duan, P., Yang, K., 2018. Mutual promotion of apoptosis and autophagy in  
748 prepubertal rat testes induced by joint exposure of bisphenol A and nonylphenol. *Environmental*  
749 *pollution* 243, 693-702.

750 Theophilou, G., Lima, K.M., Martin-Hirsch, P.L., Stringfellow, H.F., Martin, F.L., 2016. ATR-FTIR  
751 spectroscopy coupled with chemometric analysis discriminates normal, borderline and malignant  
752 ovarian tissue: classifying subtypes of human cancer. *The Analyst* 141, 585-594.

753 Wang, B., Dong, F., Chen, S., Chen, M., Bai, Y., Tan, J., Li, F., Wang, Q., 2016. Phenolic endocrine  
754 disrupting chemicals in an urban receiving river (Panlong river) of Yunnan-Guizhou plateau:  
755 Occurrence, bioaccumulation and sources. *Ecotoxicology and environmental safety* 128, 133-142.

756 Wu, J., Wang, F., Gong, Y., Li, D., Sha, J., Huang, X., Han, X., 2009. Proteomic analysis of changes  
757 induced by nonylphenol in Sprague-Dawley rat Sertoli cells. *Chemical research in toxicology* 22,  
758 668-675.

759 Xin, X., Huang, G., Liu, X., An, C., Yao, Y., Weger, H., Zhang, P., Chen, X., 2017. Molecular toxicity of  
760 triclosan and carbamazepine to green algae *Chlorococcum* sp.: A single cell view using  
761 synchrotron-based Fourier transform infrared spectromicroscopy. *Environmental pollution* 226, 12-20.

762 Yang, J., Yu, J., Wang, P., Luo, Y., Yang, X.F., Yang, X.S., Li, W.M., Xu, J., 2017. The adverse effects of  
763 perinatal exposure to nonylphenol on carbohydrate metabolism in male offspring rats. *Int J Environ*  
764 *Health Res* 27, 368-376.

765 Yang, L., Ding, Y., Chen, Y., Zhang, S., Huo, C., Wang, Y., Yu, J., Zhang, P., Na, H., Zhang, H., Ma, Y., Liu, P.,  
766 2012. The proteomics of lipid droplets: structure, dynamics, and functions of the organelle conserved  
767 from bacteria to humans. *Journal of lipid research* 53, 1245-1253.

768 Yonar, D., Ocek, L., Tiftikcioglu, B.I., Zorlu, Y., Severcan, F., 2018. Relapsing-Remitting Multiple Sclerosis  
769 diagnosis from cerebrospinal fluids via Fourier transform infrared spectroscopy coupled with  
770 multivariate analysis. *Scientific reports* 8, 1025.

771 Yousef, I., Seksek, O., Gil, S., Prezado, Y., Sule-Suso, J., Martinez-Rovira, I., 2016. Study of the  
772 biochemical effects induced by X-ray irradiations in combination with gadolinium nanoparticles in F98  
773 glioma cells: first FTIR studies at the Emira laboratory of the SESAME synchrotron. *The Analyst* 141,  
774 2238-2249.

775 Yu, J.S., Cui, W., 2016. Proliferation, survival and metabolism: the role of PI3K/AKT/mTOR signalling in  
776 pluripotency and cell fate determination. *Development* 143, 3050-3060.

777

778 **Figure legends**

779 **Figure 1. PCA-LDA of IR spectral data extracted from the testicular cells of**  
780 **rats exposed to 4-Nonylphenol (NP) at each concentration vs. control.**

781 Three-dimensional (3-D) PCA-LDA scores plots for IR spectral regions of 1800-900  
782  $\text{cm}^{-1}$  (A) and of 3200-2800  $\text{cm}^{-1}$  (B). Linear discriminant 1 (LD1) scatter plots from  
783 PCA-LDA for IR spectral regions of 1800-900  $\text{cm}^{-1}$  (C) and of 3200-2800  $\text{cm}^{-1}$  (D).  
784 Confidence ellipsoids (90%) were drawn in each 3D scores plot. The data of each  
785 LD1 scatter plot is represented as mean  $\pm$  standard deviations.  $n=6$  for each group.  
786 Significance of category segregation was determined using one-way ANOVA with  
787 the Fisher's LSD or Dunnett's T3 post-hoc test,  $***P < 0.001$  vs. the control group (0  
788 mg/kg NP).

789 **Figure 2. Cluster vectors plots comparing the control (red line at origin) and**  
790 **4-Nonylphenol (NP)-treated groups. (A) 21-day-old rats; (B) 35-day-old rats; (C)**

791 50-day-old rats. The spectra cut at 1800-900  $\text{cm}^{-1}$  (left column) were  
792 baseline-corrected and normalized to the Amide I peak prior to PCA-LDA. The  
793 spectra cut between 3100 and 2800  $\text{cm}^{-1}$  (right column) were baseline-corrected and  
794 vector-normalized. Plots were generated following PCA-LDA and show the top  
795 eight discriminating wavenumbers ( $\text{cm}^{-1}$ ) responsible for the separation between NP  
796 exposure and control groups (0 mg/kg NP). Data represent the average of six rats per  
797 group.

798 **Figure 3. Comparison of discriminating wavenumbers ( $\text{cm}^{-1}$ ) with tentative**  
799 **biomolecular assignments between control and 4-Nonylphenol (NP)-treated**

800 **groups.** IR spectra were from the testicular cells of mice exposed to different  
801 concentrations of NP. (A) Lipid-to-protein ratio (1740  $\text{cm}^{-1}$ /1400  $\text{cm}^{-1}$  ratio); (B)  
802 Peptide aggregation (1630  $\text{cm}^{-1}$ /1650  $\text{cm}^{-1}$  ratio); (C) Amide I-to-Amide II ratio  
803 (1655  $\text{cm}^{-1}$ /1545  $\text{cm}^{-1}$  ratio); (D) Phosphate-to-carbohydrate ratio [(1055-1045)  
804  $\text{cm}^{-1}$ /(1555-1535)  $\text{cm}^{-1}$  ratio]. All the data are represented as mean  $\pm$  standard  
805 deviation.  $n=6$  for each group.  $*P < 0.05$ ,  $**P < 0.01$ ,  $***P < 0.001$  vs. control group (0

806 mg/kg NP), one-way ANOVA with the Fisher's LSD or Dunnett's T3 post-hoc test.

807 **Figure 4. PCA-LDA and resultant cluster vectors plots for Raman spectra**  
808 **extracted from testicular interstitial tissue in rats treated with 4-Nonylphenol**  
809 **(NP) and untreated. (A)** Top row: 21-day-old rats. **(B)** Middle row: 35-day-old rats.  
810 **(C)** Bottom row: 50-day-old rats. Three-dimensional (3-D) PCA-LDA scores plots  
811 **(A, B and C)**, Linear discriminant 1 (LD1) scatter plots **(D, E and F)**, cluster vectors  
812 plots **(G, H and I)**, for Raman spectra region at 1800-900  $\text{cm}^{-1}$  (fingerprint region).  
813 Spectra were baseline-corrected and normalized to the Amide I peak. Confidence  
814 ellipsoids (90%) were drawn in each 3D scores plot. The data of each LD1 scatter  
815 plot is represented as mean  $\pm$  standard deviation. Cluster vectors plots were  
816 generated following PCA-LDA and show the top eight discriminating wavenumbers  
817 responsible for the separation between NP exposure and control groups. Data  
818 represent the average of six mice per group. Significance of category segregation  
819 was determined using one-way ANOVA with the Fisher's LSD or Dunnett's T3  
820 post-hoc test, \*\*\* $P < 0.001$  vs. control group (0 mg/kg NP).

821 **Figure 5. Comparison of discriminating wavenumbers ( $\text{cm}^{-1}$ ) with tentative**  
822 **biochemical assignments between control and 4-Nonylphenol (NP)-treated**  
823 **groups.** Raman spectra were from the testicular interstitial tissue of mice exposed to  
824 different concentrations of NP. **(A)** Protein-to-lipid ratio (1650  $\text{cm}^{-1}$ /1440  $\text{cm}^{-1}$  ratio);  
825 **(B)** Unsaturated lipids (1654  $\text{cm}^{-1}$ /1445  $\text{cm}^{-1}$  ratio); **(C)** Saturated lipids (1303  
826  $\text{cm}^{-1}$ /1267  $\text{cm}^{-1}$  ratio). All the data are represented as mean  $\pm$  standard deviation.  $n=6$   
827 for each group. \* $P < 0.05$ , \*\* $P < 0.01$ , \*\*\* $P < 0.001$  vs. control group (0 mg/kg NP),  
828 one-way ANOVA with the Fisher's LSD or Dunnett's T3 post-hoc test.

829 **Figure 6. PCA-LDA scores plots and resultant cluster vectors plots for IR**  
830 **spectra acquired from Sertoli cells exposed to 4-nonylphenol (NP) at various**  
831 **doses (2.5, 5, 10 and 20  $\mu\text{M}$ ) compared to the control (0  $\mu\text{M}$  NP).** Upper row:  
832 two-dimensional (2D) PCA-LDA scores plot of Linear discriminant 1 (LD1) vs.  
833 Linear discriminant 2 (LD2) **(A)**, LD1 scatter plots **(C)** and cluster vectors plots **(E)**  
834 for IR spectral region at 1800-900  $\text{cm}^{-1}$  with baseline-correction and normalization to

835 the Amide I peak ( $1650\text{ cm}^{-1}$ ). Lower row: an expanded view (**B**, **D** and **F**) of the CH  
836 stretching region  $3100\text{-}2800\text{ cm}^{-1}$ , baseline-corrected and vector-normalized.  
837 Confidence ellipsoids (90%) were drawn in each 2-D scores plot. The data of each  
838 LD1 scatter plot is represented as mean  $\pm$  standard deviation of three experiments.  
839 Cluster vectors plots were generated following PCA-LDA and show discriminating  
840 wavenumbers.  $*P < 0.05$ ,  $***P < 0.001$  vs. control group ( $0\text{ }\mu\text{M}$  NP), one-way  
841 ANOVA with the Fisher's LSD or Dunnett's T3 post-hoc test.

842 **Figure 7. Comparison of discriminating wavenumbers ( $\text{cm}^{-1}$ ) with tentative**  
843 **biochemical assignments between the control and 4-nonylphenol (NP)-treated**  
844 **Sertoli cells.** IR spectra were from Sertoli cells treated with 0, 2.5, 5, 10 and 20  $\mu\text{M}$   
845 NP for 12 h. **(A)** Lipid-to-protein ratio ( $1740\text{ cm}^{-1}/1400\text{ cm}^{-1}$  ratio); **(B)** Peptide  
846 aggregation ( $1630\text{ cm}^{-1}/1650\text{ cm}^{-1}$  ratio); **(C)** Amide I-to-Amide II ratio ( $1655$   
847  $\text{cm}^{-1}/1545\text{ cm}^{-1}$  ratio); **(D)** Phosphate-to-carbohydrate ratio [ $(1055\text{-}1045)$   
848  $\text{cm}^{-1}/(1555\text{-}1535)\text{ cm}^{-1}$  ratio]. All the data are represented as mean  $\pm$  standard  
849 deviation of three experiments.  $*P < 0.05$ ,  $**P < 0.01$ ,  $***P < 0.001$  vs. control group ( $0$   
850  $\text{mg/kg}$  NP), one-way ANOVA with the Fisher's LSD or Dunnett's T3 post-hoc test.